Sidelobe Suppression for a Steerable Parametric Source Using the Sparse Random Array Technique

Jiaxin Zhong ⓘ, *Member, IEEE*, Tao Zhuang ⓘ, Mengtong Li ⓘ, Ray Kirby ⓘ, Mahmoud Karimi ⓘ,
Jing Lu ⓘ, *Member, IEEE*, and Dong Zhang ⓘ

Abstract—A steerable parametric source is designed to steer an audio beam without mechanically rotating the source. To achieve this without the generation of grating lobes requires an ultrasonic array with interelement spacing that is less than half the wavelength of the carrier ultrasound because of the spatial Nyquist criterion. However, ultrasonic wavelengths are typically smaller than the size of an ultrasonic transducer and this generates grating lobes in the radiation pattern, which is known as the spatial aliasing effect. This work proposes a method to suppress sidelobes including these grating lobes by optimizing the position and weight coefficients of the array elements by using a sparse random array technique. This is achieved by using the peak sidelobe level as the objective function and the simulated annealing algorithm for the optimization. Both simulation and experimental results demonstrate the sidelobe level can be effectively suppressed when the average interelement spacing is two wavelengths. It is also found that Westervelt directivity has a significant effect on the spatial aliasing, because it serves as a spatial filter on the product directivity of the ultrasound. Accordingly, the sidelobe suppression performance deteriorates at low audio frequencies and high ultrasound frequencies where Westervelt directivity tends to be broader. However, this deterioration in performance can be addressed by increasing the number of the array elements.

Index Terms—Parametric array loudspeaker, parametric source, directional audio beam, steerable beam, sidelobe suppression, grating lobe suppression, simulated annealing, sparse array.

I. INTRODUCTION

PARAMETRIC array loudspeakers (PALs) have been widely used in many audio applications due to their ability of generating highly directional sound beams [1]. The steerable PAL adopts the phased array technique that provides advantages over conventional PALs for steering directional audio beams in a desired direction without the need to mechanically rotate the source. Its mechanism and properties have been extensively studied and this has seen applications in active noise control [2], sound reproduction systems [3], and so on. A steerable PAL is usually constructed by arranging a linear ultrasonic transducer array and applying the phased array technique. This is designed to generate a low sidelobe and a grating lobe free audio beam. However, the wavelength of the carrier ultrasound (usually 4.3 mm at 40 kHz) is so small compared to the size of available ultrasonic transducers (usually 10 mm) that it is difficult to satisfy the Nyquist criterion, which requires that the interelement spacing is smaller than half wavelength. Although there are many preprocessing techniques proposed to eliminate the resulting distortion [4], [5], [6], [7], few studies are concerned with addressing the spatial aliasing issue. To address this, it is proposed to optimize the design of a steerable PAL using a sparse random array technique to suppress the sidelobes when the Nyquist criterion is not satisfied.

When a PAL radiates an intensive ultrasound at two frequencies, audio sound at the difference frequency is generated due to the nonlinear interactions of the ultrasounds. A PAL radiating a pure-tone audio signal is commonly referred to as a parametric source. The audio sound field generated by a parametric source is so complicated that appropriate approximations must be assumed to obtain numerical predictions. A quasilinear approximation is usually valid and this simplifies the physical modelling because the pressure levels of ultrasonic waves are limited for safety concern [1]. Under this framework, the sound fields generated by a parametric source can be divided into three regions: the near field, the Westervelt far field, and the inverse-law far field [8]. In the near field, the audio sound experiences strong local effects resulting in many local maxima and minima in the sound pressure. Several methods have been proposed to model the audio sound in the near field, although they demand heavy computational expenditure [8], [9], [10]. The Westervelt far field means the region where the Westervelt equation is sufficiently accurate, and the audio sound can be calculated more efficiently with various kinds of methods proposed in the literature [11], [12], [13], [14].

This work focuses on suppressing sidelobes present in the inverse-law far field, where the audio sound pressure is inversely proportional to the propagation distance. This requires the

observation point to be far enough away from the absorption distance of the parametric source [8]. Using the audio sound directivity in the inverse-law far field, it is straightforward to characterize the radiation pattern of a steerable parametric source. A closed-form expression for directivity was first obtained by Westervelt, and is now termed Westervelt directivity [15]. The expression shows that the directivity has no sidelobe and is affected only by the audio frequency and the ultrasound attenuation coefficient due to atmospheric absorption. The accuracy of Westervelt directivity was then improved by Berktay and Leahy by taking into account the aperture factor and the wave shape [16], [17]. The product directivity model was more convenient to use when calculating the directivity of a steerable parametric source, which approximates the audio sound directivity by the product of the directivity of two ultrasonic waves [18]. The sidelobe level predicted by the product directivity model was found to be much smaller than measurements because the diffraction of audio sound waves was neglected in the model, although this can be addressed to some extent by using an equivalent Gaussian source array [19]. Recently, a convolution model was proposed which obtains the audio sound directivity by calculating the convolution between Westervelt directivity and the product of the ultrasonic directivities [20], [21], [22]. The convolution model provides better agreement with measurement and it also has relatively low computational cost, and so this will be used in the current work to obtain the directivity.

The steerable parametric source realized by a uniform array configuration, where the interelement spacing between adjacent transducers is identical, has been extensively investigated [18], [23], [24]. Since Nyquist criterion is hard to satisfy, grating lobes in the ultrasound directivity are inevitably generated. It is interesting to note that the audio sound may not fully inherit the grating lobe from the ultrasound. The locations of grating lobes of two ultrasound waves are separated due to different wavelengths. When the separation is sufficiently large, the product directivity of ultrasound is small, resulting in low levels of audio beams in this direction, which is known as the grating lobe elimination phenomenon [23]. This phenomenon has been utilized to steer dual beams using only one steerable parametric source [24]. However, in most cases the grating lobe can only be partially suppressed when adopting a uniform array. In addition, Westervelt directivity is not taken into account in the analysis of [23]. It characterizes the effective length and the diffraction ability of the virtual audio sound source, and serves as a spatial filter on the product directivity of the ultrasound. At low audio frequencies and high ultrasound frequencies, Westervelt directivity tends to be broader, so it may result in more aliasing effects.

The sparse random array technique is a promising approach to suppressing grating lobes, where "sparse" means the average interelement spacing is larger than half wavelength and "random" means the elements are unequally spaced so that the sound waves emitted from the array elements arrive randomly at the grating lobe, although they do arrive in-phase at the main lobe [25]. To the best of authors' knowledge, the sparse random array has not been applied in the design of a steerable parametric source. However, it has been successfully used in designing
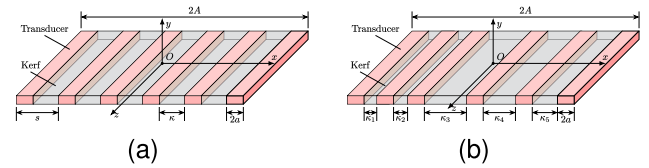

Fig. 1. Sketch of the steerable parametric source consisting of N (6 in this figure) ultrasonic transducer elements with a width $2a$: (a) uniform array with the equal interelement spacing; (b) random array with the unequal interelement spacing.

antenna [26] and medical ultrasound [25] arrays. For example, the peak sidelobe level can be suppressed by more than 12 dB in a typical configuration consisting of 25 array elements over an aperture of 50 wavelengths [27]. Apart from the position of the elements, the weight coefficients can also be optimized to further improve the suppression performance by reducing the sidelobe level. There are several well-developed algorithms to obtain the optimal configurations of a sparse array, including simulated annealing (SA) [27], genetic algorithms [28], differential evolution algorithms [27], and particle swarm optimization [29]. SA is the most commonly used approach because it is a stochastic approach to solving combinatorial optimization problems with the ability of escaping local minima of the objective function [30], [31]. Accordingly, in this work, SA is used for the first time to suppress the sidelobe as well as the grating lobe of a steerable parametric source.

In this article, the audio sound directivity is modelled using the convolution model for its computational efficiency [21]. The grating lobes generated by a linear parametric source array are suppressed by optimizing the position and weight coefficients of the array elements using the SA algorithm. The directivity generated by the optimal array is compared to that by a uniform array. A parametric study is then conducted to investigate the dependence on the audio frequency, ultrasound frequency, and the number of elements. Finally, experiments are conducted using a steerable parametric source to validate the simulation results.

II. THEORY

Fig. 1 shows two configurations of a steerable parametric source consisting of N linear array elements. A Cartesian coordinate system $Oxyz$ is established with its origin at the centroid of the array and the y-axis perpendicular to the radiation surface. For simplicity, the size of all array elements in the x-direction is set as the same and denoted by $2a$. The size of all elements in the z-direction is assumed to be much larger than the wavelength so that the radiation can be modelled only in the two-dimensional plane Oxy [32]. Fig. 1(a) presents the uniform array configuration where the interelement spacing (also known as the array pitch) is identical and denoted by s. The kerf width is denoted by κ and the total kerf width is obtained as $\kappa_{\text{tot}} = (N-1)\kappa$. Fig. 1(b) shows the random array configuration where the interelement spacing is randomly chosen, and the kerf width between the n-th and $(n+1)$-th elements is denoted by κ_n, where $n = 1, 2, \ldots, N-1$. Without loss of generality, the total kerf width in Fig. 1(b) is restricted

as $(N-1)\kappa$, so that the average kerf and interelement spacing is equal to κ and s, respectively. The term "sparse" means the average interelement spacing is larger than half wavelength of the carrier ultrasound, so that Nyquist criterion is not satisfied and grating lobes are present in the radiation pattern. The total size of the array is denoted by $2A$ and can be obtained for both configurations as

$$A = \frac{(N-1)s}{2} + a. \tag{1}$$

A. Audio Sound Directivity

When the ultrasound at the frequencies of f_1 and f_2 ($f_1 > f_2$) is radiated by the parametric source, the audio sound with a frequency $f_a = f_1 - f_2$ is demodulated in air due to the second-order nonlinearity caused by air. In this article, the audio sound directivity in the inverse-law far field is calculated using the convolution model [14], [21]

$$\mathcal{D}(\varphi) = [\mathcal{D}_1(\varphi)\mathcal{D}_2^*(\varphi)] * \mathcal{D}_W(\varphi)$$
$$= \int_0^\pi \mathcal{D}_1(\varphi')\mathcal{D}_2^*(\varphi')\mathcal{D}_W(\varphi - \varphi')\mathrm{d}\varphi', \tag{2}$$

where the azimuthal angle $\varphi = \operatorname{atan2}(y, x)$, which is the angle between the positive x-axis and the ray from the origin to the point (x, y), the operator $*$ denotes the linear convolution, and the superscript $*$ denotes the complex conjugate. The ultrasound directivity at the frequency f_i generated by the array is given as, see (4.26) in [33]

$$\mathcal{D}_i(\varphi) = \mathcal{D}_a(\varphi, k_i)\mathcal{D}_s(\varphi, k_i), \tag{3}$$

where $k_i = \omega_i/c_0 + \mathrm{i}\alpha_i$ is the wavenumber of the ultrasound, $\omega_i = 2\pi f_i$, $i = 1$ and 2, c_0 is the linear sound speed, and α_i is the attenuation coefficient at the frequency f_i due to atmospheric absorption [34]. The element directivity $\mathcal{D}_a(\varphi, k_i)$ and the discrete point source directivity $\mathcal{D}_s(\varphi, k_i)$ are, respectively,

$$\mathcal{D}_a(\varphi, k_i) = \operatorname{sinc}(k_i a \cos \varphi), \tag{4}$$

$$\text{and } \mathcal{D}_s(\varphi, k_i) = \sum_{n=1}^N w_n \exp[-\mathrm{i}k_i x_n(\cos\varphi - \cos\varphi_0)]. \tag{5}$$

In (5), w_n and x_n represent the weight coefficient and the x-coordinate of the centroid of the n-th element, respectively, and φ_0 is the steering angle. The special case when $\varphi_0 = \pi/2$ ($90°$) represents a conventional parametric source without beam steering. The Westervelt directivity in (2) is [15]

$$\mathcal{D}_W(\varphi) = \frac{1}{1 - \mathrm{i}k_a\alpha_u^{-1}\sin^2(\varphi/2)}, \tag{6}$$

where $k_a = \omega_a/c_0$ is the audio wavenumber, $\omega_a = 2\pi f_a$, f_a is the audio frequency, and the average ultrasonic attenuation coefficient $\alpha_u = (\alpha_1 + \alpha_2)/2$.

B. Uniform Array

The uniform array shown in Fig. 1(a) is the fundamental configuration, so its performance will be used for comparison in this article. In this configuration, the x-coordinate of the centroid of the n-th element is

$$x_n = \left(n - \frac{N+1}{2}\right)s. \tag{7}$$

By using (7), the discrete point source directivity given by (5) can be further reduced to, see (4.28) in [33]

$$\mathcal{D}_s(\varphi, k_i) = \frac{\sin[Nk_i s(\cos\varphi - \cos\varphi_0)/2]}{N\sin[k_i s(\cos\varphi - \cos\varphi_0)/2]}. \tag{8}$$

Grating lobes are present when the following condition is satisfied, see (4.29) in [33]

$$k_i s(\cos\varphi_m - \cos\varphi_0) = 2m\pi, \quad m = \pm 1, \pm 2, \pm 3, \ldots, \tag{9}$$

where the angle of the grating lobe, φ_m, is obtained as

$$\varphi_m = \operatorname{acos}\left(\cos\varphi_0 + \frac{m\lambda_i}{s}\right). \tag{10}$$

One can see that if the interelement spacing $s > \lambda_i/2$ then the array generates at least one grating lobe at an angle φ_m. However, it is worth noting that the audio sound may not fully inherit the grating lobes from the ultrasound calculated by (10), which is termed the grating lobe elimination phenomenon and has been investigated in [23]. The reason is that the audio sound directivity is affected by the product of the directivity of two ultrasonic waves, as shown in (2). When the locations of grating lobes of two ultrasonic waves are separated, their product can be small enough to be ignored. For example, using the parameters in Fig. 6(b) of [23], when the sound beam is steered at the angle of $105°$ with the ultrasound frequencies of 40 kHz and 50 kHz, and an interelement spacing of 17.15 mm, (10) predicts the first grating lobe ($m = 1$) to be located at $76.0°$ and $81.9°$. Due to a separation of $5.9°$ for these grating lobes, the product directivity of them is small at this direction. However, the audio sound directivity is also affected by Westervelt directivity, as shown in (2), although this was not considered in [23]. The Westervelt directivity characterizes the effective length and the diffraction ability of the virtual audio source, and its effects on the radiation pattern of the steerable parametric source will be demonstrated in Section III.

C. Optimal Array Obtained Using Simulated Annealing

SA is a stochastic based algorithm for the global optimization problem, which provides a good approximation of the global optimum for an objective function defined on a large parameter space [30]. To minimize both the grating lobe and sidelobe levels, the objective function is chosen here as the maximal magnitude of the audio sound directivity for the angles outside of the main lobe, as a function of an element's position and weight coefficients, so that [35]

$$J(\mathbf{x}, \mathbf{w}) = \max_{\varphi, \text{s.t.}|\varphi - \varphi_0| \geq \Delta\varphi} |\mathcal{D}(\varphi)|, \tag{11}$$

where $\Delta\varphi > 0$ is set to cover the main lobe, the element position vector $\mathbf{x} = [x_1, x_2, \ldots, x_N]^\mathrm{T}$, the weight coefficient vector $\mathbf{w} = [w_1, w_2, \ldots, w_N]^\mathrm{T}$, and the superscript "T" denotes a matrix transpose. The level of (11), i.e., $20\log_{10}(J)$, is known

Algorithm: Simulated Annealing

Input : $T_0, \mathbf{d}, \mathbf{x}, \mathbf{w}, w_{\min}, w_{\max}, \gamma, \sigma_d, \sigma_w$

Output: $E_{\text{best}}, \mathbf{x}_{\text{best}}, \mathbf{w}_{\text{best}}$

$d_0^{\dagger} = 0; d_n^{\dagger} = \kappa_{\text{tot}}; x_1^{\dagger} = a - A$;　　　/* Initialization */

$E_{\text{best}} = E = J(\mathbf{x}, \mathbf{w})$;

for $j = 1$ **to** $j_{\max}$ **do**　　　　　　/* Iterations */

　　$T_j = \gamma T_{j-1}$;　　　　　　　/* Cooling */

　　/* Perturb the kerf widths　　　　*/
　　for $n = 1$ **to** $N - 2$ **do**
　　　　$d_n^{\dagger} = \text{mod}\,(\mathcal{N}(d_n, \sigma_d^2), \kappa_{\text{tot}})$;

　　/* Obtain x-coordinates of the elements　*/
　　for $n = 1$ **to** N **do**
　　　　$x_n^{\dagger} = x_{n-1}^{\dagger} + 2a + d_n^{\dagger} - d_{n-1}^{\dagger}$

　　/* Perturb the weight coefficients　*/
　　for $n = 1$ **to** N **do**
　　　　$w_n^{\dagger} = \text{mod}\,(\mathcal{N}(w_n - w_{\min}, \sigma_w^2), w_{\max} - w_{\min}) + w_{\min}$;

　　$E^{\dagger} = J(\mathbf{x}^{\dagger}, \mathbf{w}^{\dagger})$;　　　/* Obtain new energy */

　　$\Delta E = E^{\dagger} - E$;　　　　　/* Energy difference */

　　if $(\Delta E < 0)$ or $(\mathcal{U}(0,1) < e^{-\Delta E/T_j})$ **then**
　　　　$\mathbf{d} = \mathbf{d}^{\dagger}; \mathbf{w} = \mathbf{w}^{\dagger}; E = E^{\dagger}$;　/* Accept result */

　　if $E^{\dagger} < E_{\text{best}}$ **then**　　　/* Update best result */
　　　　$\mathbf{x}_{\text{best}} = \mathbf{x}^{\dagger}; \mathbf{w}_{\text{best}} = \mathbf{w}^{\dagger}; E_{\text{best}} = E^{\dagger}$

Fig. 2. Implementation of the SA algorithm for optimizing the steerable parametric source.

TABLE I
THE PARAMETERS USED IN SIMULATIONS

Symbol	Definition	Value
a	Half width of the element	5 mm
$j_{\max}$	Maximal iteration numbers	10,000
s	Average interelement spacing	17.15 mm
T_0	Initial temperature in SA	10
$w_{\min}$	Minimum of the weight coefficient	0.2
$w_{\max}$	Maximum of the weight coefficient	2
γ	Decay rate in the cooling schedule	0.95
σ_d	Standard deviation for position	$\kappa_{\text{tot}}/6$
σ_w	Standard deviation for weight coefficients	0.3
φ_0	Steering angle	70°
$\Delta\varphi$	Beam width of the main lobe	25°

An exponential schedule is adopted here, so that [31]

$$T_j = \gamma T_{j-1}, \quad j = 1, 2, \ldots, j_{\max} \tag{13}$$

with a cooling factor $\gamma \in (0, 1)$, where j is the iteration index and $j_{\max}$ is the maximal iteration number. At each iteration, the points $d_1, \ldots, d_{N-2}$ are perturbed as $d_1^{\dagger}, \ldots, d_{N-2}^{\dagger}$ subject to the normal distribution $\mathcal{N}(d_n, \sigma_d^2)$, with mean d_n and standard deviation σ_d. The modulo operation $\text{mod}\,(\mathcal{N}(d_n, \sigma_d^2), \kappa_{\text{tot}})$ is used to ensure the result is less than κ_{tot}, where $\text{mod}\,(\xi_1, \xi_2)$ is defined by the floor function $\lfloor \cdot \rfloor$ as $\xi_1 - \xi_2 \lfloor \xi_1/\xi_2 \rfloor$. The perturbed results $d_1^{\dagger}, \ldots, d_{N-2}^{\dagger}$ are sorted to ensure a non-decreasing order. The new position vector $\mathbf{x}^{\dagger}$ is then obtained according to the perturbed vector $\mathbf{d}^{\dagger}$. Meanwhile, the weight coefficients $w_1, \ldots, w_N$ are perturbed as $w_1^{\dagger}, \ldots, w_N^{\dagger}$ and subject to a normal distribution with standard deviation σ_w. The objective function with perturbed results is evaluated as $E^{\dagger} = J(\mathbf{x}^{\dagger}, \mathbf{w}^{\dagger})$. If the energy is decreased, i.e., $\Delta E < 0$, then the new perturbed parameters are accepted. If the energy is increased, i.e., $\Delta E > 0$, then the parameters are accepted with a probability dependent on the temperature at this iteration, T_j. In this article, the parameters are accepted when a random number generated based on a standard uniform distribution $\mathcal{U}(0, 1)$ is less than $e^{-\Delta E/T_j}$. The lower the temperature is, the lower the possibility that a worse configuration can be accepted.

as the peak sidelobe level (PSL) and is used as a metric in this article to quantify the performance of the array. The optimization problem is to find the global minimum of the objective function by optimizing $\mathbf{x}$ and $\mathbf{w}$.

Appropriate restrictions on the position and weight coefficients of array elements are required during the optimization procedure. Accordingly, the weight coefficients are restricted in the interval $[w_{\min}, w_{\max}]$. The total size of the array, $2A$, is fixed *a priori* indicating that $x_1 = a - A$, $x_N = A - a$, and the total kerf width, κ_{tot}, is then fixed as $2A - 2Na$. As shown in Fig. 1(b), it is necessary that for all kerf widths, $\kappa_n \geq 0$, so that the spacing between adjacent elements is no less than the element size, $2a$. We then define a partition of the interval $[0, \kappa_{\text{tot}}]$ as

$$\mathcal{P} = \{0 = d_0 \leq d_1 \leq \cdots \leq d_{N-1} = \kappa_{\text{tot}}\}, \tag{12}$$

which breaks up the allowed total kerf width into $N - 1$ subintervals. The n-th subinterval is $[d_{n-1}, d_n]$, the length of which is equal to the kerf width between the n-th and the $(n+1)$-th element, with $\kappa_n = d_n - d_{n-1}$, where $n = 1, 2, \ldots, N - 1$. Because the total array size is fixed at $2A$, the kerf width κ_n is restricted in the range $[0, 2A - 2Na]$. Consequently, the optimization of the vector $\mathbf{d} = [d_0, d_1, \ldots, d_{N-1}]^{\text{T}}$ is equivalent to the optimization of the element position vector $\mathbf{x}$.

The implementation of SA procedure is illustrated in Fig. 2. An initial temperature, T_0, is chosen to be high enough so that the first perturbation can be accepted with a high possibility. The initial position and weight coefficient vectors are then arbitrarily set, and the temperature cools down at each iteration.

III. SIMULATIONS

Numerical simulations are conducted using MATLAB R2022a. The sound attenuation coefficient due to atmospheric absorption is calculated according to ISO 9613-1 [34], with a relative humidity of 70% and temperature 20 °C. For simplicity, some parameters are fixed and listed in Table I. Without loss of generality, the directivities presented in the following text are normalized to be equal to unity in the steering direction φ_0.

A. Performance of the Optimal Sparse Random Array

Fig. 3 shows both the ultrasound and audio sound directivities generated by a uniform array consisting of $N = 8$ elements at the audio frequency $f_a = 2$ kHz, where the interelement spacing is $s = 17.15$ mm, and the steering angle $\varphi_0 = 70°$. Since the interelement spacing is larger than half a wavelength, three grating lobes are present, as shown in the top row of Fig. 3, the
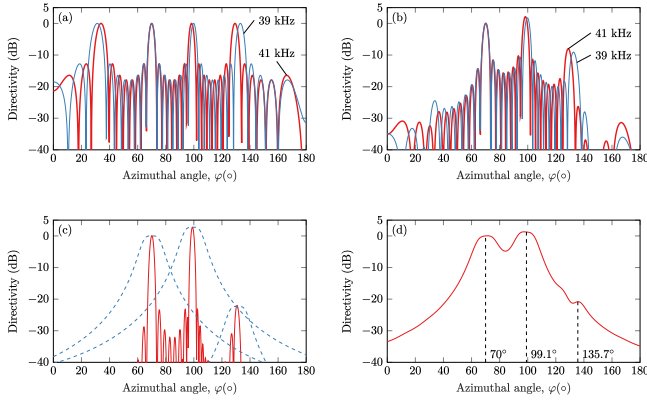
Fig. 3. Directivities generated by a uniform array where the element number $N = 8$, the audio frequency $f_a = 2$ kHz, and the average ultrasound frequency $f_u = 40$ kHz: (a) the discrete point source directivity and (b) the total array directivity for ultrasound; red solid line, $f_1 = 41$ kHz; blue solid line, $f_2 = 39$ kHz. (c) Red solid line, the product directivity of ultrasound; blue dashed line, Westervelt directivity. (d) The audio sound directivity.
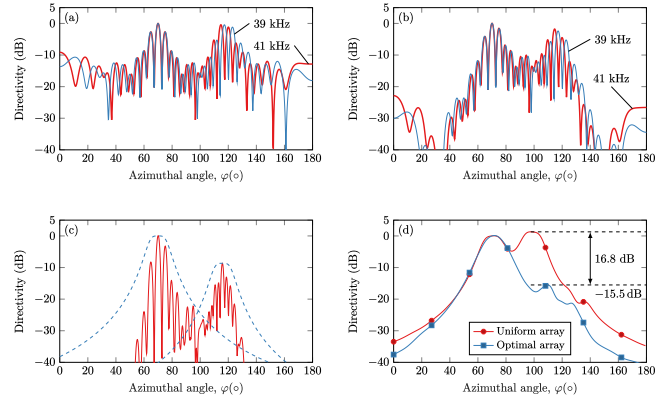

Fig. 4. Directivities generated by an optimal array, where the element number $N = 8$, the audio frequency $f_a = 2$ kHz, and the average ultrasound frequency $f_u = 40$ kHz: (a) the discrete point source directivity and (b) the total array directivity for ultrasound; red solid line, $f_1 = 41$ kHz; blue solid line, $f_2 = 39$ kHz. (c) Red solid line, the product directivity of ultrasound; blue dashed line, Westervelt directivity. (d) The audio sound directivity.

TABLE II
THE POSITION AND WEIGHT COEFFICIENTS FOR THE UNIFORM AND OPTIMAL ARRAY CONFIGURATIONS PRESENTED IN FIGS. 3 AND 4

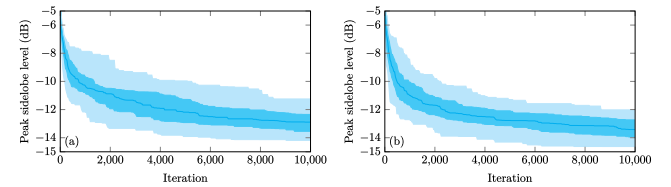| Element index, n	Position, x_n (mm)		Weight coefficients, w_n	
	Uniform array	Optimal array	Uniform array	Optimal array
1	−60	−60	1	1.99
2	−43	−49	1	1.17
3	−26	−39	1	1.15
4	−9	−28	1	0.92
5	9	−17	1	0.62
6	26	40	1	1.19
7	43	50	1	1.73
8	60	60	1	1.51

Fig. 5. Optimized PSL as a function of the number of SA iterations based on 100 trials where the element number $N = 8$, the audio frequency $f_a = 2$ kHz, and the average ultrasound frequency $f_u = 40$ kHz: (a) optimizing only the position; (b) optimizing both the position and weight coefficients. Here and in the sequel, the blue regions indicate the 5% to 95% and 25% to 75% empirical Gaussian quantiles of the PSL. The blue solid line denotes the median value.

locations of which can be predicted using (10). Fig. 3(b) demonstrates the importance of considering the element directivity of ultrasound, as described by (4) which was not considered in [23]. The element directivity is controlled by the non-dimensional wavenumber, $k_i a$. The radiation pattern is nearly uniform when $k_i a$ is small so that the effects can be ignored. However, the size of ultrasonic transducers (10 mm) used in a steerable parametric source is usually larger than the wavelength (8.7 mm at 40 kHz) resulting in a highly directional element directivity [24], so that the grating lobe observed at $32.6°$ is sufficiently small to be ignored. Fig. 3(c) presents the product directivity of the ultrasound and the envelopes of Westervelt directivity at the main lobe, and two grating lobes at $99.1°$ and $130.8°$. After the convolution process in (2), the audio sound directivity is obtained as shown in Fig. 3(d). It can be observed that except for the main lobe at $70°$, there are two other peaks around $99.1°$ and $135.7°$, which represent two grating lobes with levels of 1.3 dB and $−20.8$ dB, respectively.

The advantage of the sparse random array is shown in Fig. 4, where the directivities are calculated according to an optimal array configuration after optimizing both the element position and weight coefficients using the SA algorithm. The average interelement spacing is two wavelengths of the ultrasound, i.e., $s = 17.15$ mm, and other parameters are the same as those used in Fig. 3. The optimal parameters are presented in Table II. It

can be observed in the top row of Fig. 4 that only the grating lobes around $120°$ are retained and the levels become smaller. Moreover, in Fig. 4(c) the peaks in the two ultrasonic waves around $120°$ are seen not to coincide with each other so that their product is further suppressed. In this typical configuration, the PSL is reduced to $−15.5$ dB, as shown in Fig. 4(d). By comparison with the directivity obtained using the uniform array, the grating lobe is suppressed by 16.8 dB. The results validate the feasibility of using the SA to suppress the sidelobe as well as the grating lobe generated in a uniform array.

Fig. 5 shows the optimized PSL as a function of the number of SA iterations after optimizing only the position, and then the position and weight coefficients, where the parameters are the same as those used in Fig. 4. The results are obtained based on 100 trials, and hereafter the light blue and dark blue regions indicate 5% to 95%, and 25% to 75% for the empirical Gaussian quantiles of the PSL, respectively. The blue solid line denotes the median value. In a personal computer with an AMD Ryzen Threadripper 3960X (Santa Clara, CA) central processing unit (CPU) with 256 GB of random access memory (RAM), the calculation time is around 160 s for 10,000 iterations. It is observed the PSL converges to small values for both cases, and the median and best results are, respectively, $−12.9$ dB and $−14.4$ dB when optimizing only the position, as shown in Fig. 5(a).
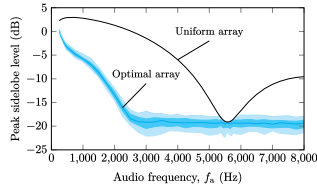
Fig. 6. Statistical results of the PSL of the optimal array based on 100 trials after 10,000 iterations, where the element number $N = 8$, and the average ultrasound frequency $f_u = 40$ kHz. The black solid line represents the PSL obtained using the uniform array.
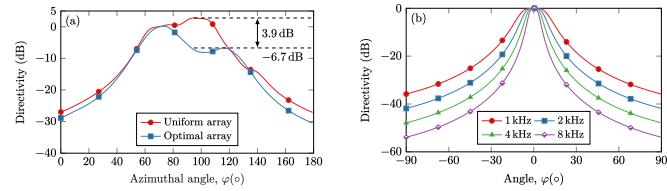

Fig. 7. (a) The comparison of the audio sound directivity generated by a uniform array and an optimal array at the audio frequency $f_a = 1$ kHz, where the element number $N = 8$. (b) The Westervelt directivity at different audio frequencies. The average ultrasound frequency $f_u = 40$ kHz.
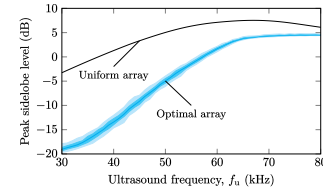

Fig. 8. Statistical results of the PSL of the optimal array based on 100 trials after 10,000 iterations at different average ultrasonic frequencies, where the element number $N = 8$, and the audio frequency $f_a = 2$ kHz.
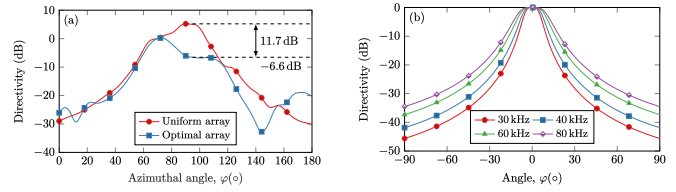

Fig. 9. (a) The comparison of the audio sound directivity generated by a uniform array and an optimal array when the average ultrasound frequency $f_u = 50$ kHz, where the element number $N = 8$. (b) The Westervelt directivity at different audio frequencies. The audio frequency $f_a = 2$ kHz.

They can be further reduced to -13.4 dB and -15.5 dB, respectively, by optimizing both the position and the weight coefficients. Although the weight coefficients cannot reduce the presence of grating lobes, they provide more degrees of freedom to improve suppression performance by reducing sidelobe levels [27]. To obtain better performance, all the following results optimize both the position and weight coefficients.

B. Effects of the Audio Frequency

Fig. 6 shows the statistical results of the PSL after 10,000 iterations based on 100 independent trials at different audio frequencies, ranging from 250 Hz to 8 kHz. The black solid line represents the PSL obtained using the uniform array. It can be found that the PSL generated by a uniform array generally decreases as the audio frequency increases and reaches its minima at around 5.6 kHz. However, the PSL generated by the optimal array decreases as the frequency increases and converges to around -20 dB. The audio sound directivity at 1 kHz is also shown in Fig. 7(a), and when compared to the result at 2 kHz in Fig. 4(d) the PSL is suppressed to only -6.7 dB, which means that it is more difficult to suppress the sidelobes at low frequencies. The reason for this can be observed in Fig. 7(b), where Westervelt directivities are presented at several audio frequencies with the same average ultrasonic frequency of 40 kHz. The half power beam width (HPBW) of Westervelt directivity increases from $7.3°$ to $10.3°$, then to $14.6°$, and finally to $20.6°$ as the frequency decreases from 8 kHz to 4 kHz, 2 kHz, and 1 kHz, respectively. The larger HPBW at lower frequencies described by (6) results in more aliasing effects so that the suppression performance for sidelobes is deteriorated. In the high frequency range, the HPBW of the Westervelt directivity is small so that the audio sound directivity can be optimized more effectively.

It is interesting to note that the PSL generated by a uniform array reaches its minima at around 5.6 kHz. As the audio frequency increases, the difference of the two ultrasonic frequencies increases, so the angular separation of grating lobes between these two ultrasonic waves becomes larger. The level of the product directivity of these two ultrasonic waves is then decreased, resulting in a lower level for the audio sound directivity. This is known as the grating lobe elimination phenomenon in a steerable parametric source, and it is discussed in detail in [23]. However, the PSL generated by the optimal array shown in Fig. 6 is found to be lower than that without the optimization (uniform array) in the frequency range from 250 Hz to 8 kHz. It means that the uniform array is never the optimal configuration for the parameters used in Fig. 6. Thus, by optimizing the array using the SA algorithm, the grating lobe can always be suppressed.

C. Effects of the Ultrasound Frequency

Fig. 8 shows the statistical results of the PSL for an optimal array after 10,000 iterations based on 100 independent trials at different average ultrasound frequencies ranging from 30 kHz to 80 kHz. It can be found that the PSL generally increases as the ultrasound frequency increases, for both uniform and optimal array configurations. Fig. 9(a) shows a comparison between the directivity obtained using uniform and optimal arrays when the ultrasound frequency is 50 kHz. Compared to Fig. 4(d), when the ultrasound frequency is 40 kHz, it is found that the suppression of the grating lobe decreases from 16.8 dB to 11.7 dB. The reason can be explained by comparing Westervelt directivity at different ultrasound frequencies, as shown in Fig. 9(b). Because the attenuation coefficient increases monotonically with the ultrasound frequency [34], Westervelt directivity is broader at higher frequencies, as shown by (6). The HPBW increases from $11.7°$ to $14.6°$, then to $18.9°$, and finally to $22.3°$ as the
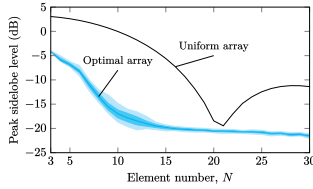
Fig. 10. Statistical results of the PSL of the optimal array based on 100 trials after 10,000 iterations for the array consisting of N elements, where the audio frequency $f_a = 2\,\text{kHz}$ and the average ultrasound frequency $f_u = 40\,\text{kHz}$.
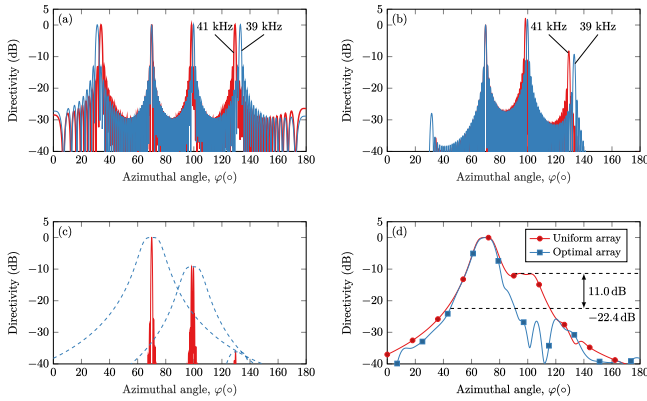

Fig. 11. Directivities generated by a uniform array where the element number $N = 30$, the audio frequency $f_a = 2\,\text{kHz}$, and the average ultrasound frequency $f_u = 40\,\text{kHz}$: (a) the discrete point source directivity and (b) the total array directivity for ultrasound; red solid line, $f_1 = 41\,\text{kHz}$; blue solid line, $f_2 = 39\,\text{kHz}$. (c) Red solid line, the product directivity of ultrasound; blue dashed line, Westervelt directivity. (d) The audio sound directivity.

frequency increases from 30 kHz to 40 kHz, 60 kHz, and 80 kHz, respectively. This behavior is caused by a narrow audio beam that is generated by the effective virtual source, which is determined by the absorption length, $1/\alpha_u$. At small absorption lengths, the effective length of the virtual source is small so that it is unable to generate a narrow beam. Therefore, it is more difficult to suppress the grating lobe at higher ultrasound frequencies.

D. Effects of the Number of Elements

Fig. 10 shows the statistical results of the PSL for the uniform and optimal arrays at different numbers of elements, where the audio frequency $f_a = 2\,\text{kHz}$ and the average ultrasound frequency $f_u = 40\,\text{kHz}$. It is interesting to note that the PSL for the uniform array decreases as the element number increases, reaching the local minimum at $N = 21$, and then increasing up to $N = 30$. This is different when compared to a uniform array consisting of conventional loudspeakers, the PSL of which is known to be independent of the element number. This can be explained by comparing Figs. 3 and 11, where the directivities of both ultrasound and audio sound are presented for a uniform array, when the array number $N = 30$. Although the angular separation of the grating lobes around $130°$ for the two ultrasound waves is the same $(3.8°)$, the grating lobes become sharper when the element number increases from 8 to 30, which can be derived from (8). Therefore, the product directivity becomes smaller by
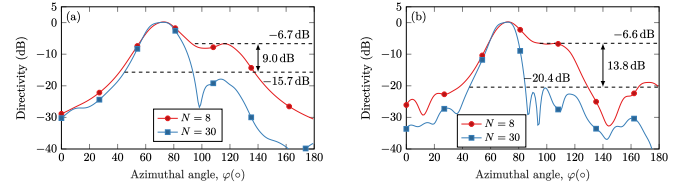

Fig. 12. Comparison of the audio sound directivity generated by the optimal array when the element number $N = 8$ or 30: (a) the audio frequency $f_a = 1\,\text{kHz}$ and the average ultrasound frequency $f_u = 40\,\text{kHz}$; and (b) the audio frequency $f_a = 2\,\text{kHz}$ and the average ultrasound frequency $f_u = 50\,\text{kHz}$.

comparison in Figs. 3(c) and 11(c). This can be attributed to the grating lobe elimination phenomenon, although this was not discussed in [23]. This also benefits the suppression performance for the optimal array, as we can see in Fig. 10 where the PSL of the optimal array is seen to monotonically decrease as the element number increases. Meanwhile, it is also concluded that the uniform array can always be optimized to have lower PSLs. For example, the PSL can be further reduced by 11.0 dB when the element number $N = 30$ as shown in Fig. 11(d).

The above results suggest it is possible to improve suppression performance at low audio frequencies and/or high ultrasound frequencies, which have been shown difficult to optimize in Section III-B and III-C. Fig. 12 shows the audio sound directivity generated by an optimal array when the element number is 8 or 30. By comparing Figs. 12(a) and 7(a), it can be found the PSL can be further reduced from -6.7 dB to -15.7 dB, with an improvement of 9.0 dB when the audio frequency is 1 kHz and the average ultrasound frequency is 40 kHz. By comparing Figs. 12(b) and 9(a), the PSL is further reduced from -6.6 dB to -20.4 dB with an improvement of 13.8 dB when the audio frequency is 2 kHz and the average ultrasound frequency is 50 kHz. In conclusion, adding more array elements can increase the suppression of sidelobes and grating lobes at both low audio and high ultrasound frequencies.

IV. EXPERIMENTS

To validate the theory presented in previous sections, eight steerable parametric sources with uniformly and optimally distributed elements were fabricated for generating audio sound at 1 kHz or 2 kHz, and two of them are shown in Figs. 13(a) and (b). The parametric sources consist of 8 or 16 channels with 8 circular ultrasonic emitters in each channel (Murata MA40S4S, Kyoto, Japan), with a resonance frequency of 40 kHz and a diameter of 1 cm. The average interelement spacing of all parametric sources is two wavelengths of ultrasound, i.e., $s = 17.15\,\text{mm}$. The position and weight coefficients for the uniform and optimal array configurations with 8 channels at 2 kHz are adopted from the simulation results given by Table II. The position and weight coefficients for other configurations are not presented for the sake of conciseness.

The steerable parametric source is realized by a field programmable gate array (FPGA, Xilinx XC7A100 T, San Jose, CA) and metal-oxide semiconductor field-effect transistor
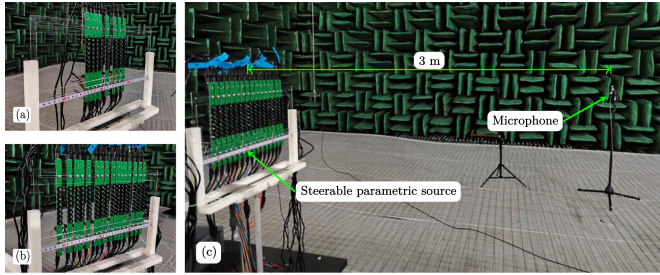
Fig. 13. Prototypes of the (a) 8-channel and (b) 16-channel parametric source with optimally distributed elements at (a) 1 kHz and (b) 2 kHz, respectively, where each channel consists of 8 ultrasonic elements. (c) Photo of the experimental setup with a uniform 16-channel array.

(MOSFET) drivers (Microchip MIC4127, Chandler, AZ). The logical diagram of the circuits is the same as Fig. 8 in [36]. The FPGA is programmed to generate multi-channel independent rectangular pulse signals which are fed into the corresponding MOSFET drivers, whose output is connected to the positive pins of the ultrasonic emitters [37]. The signal at each channel consists of two pulse signals at two ultrasonic frequencies of 40 kHz and 40.98 kHz (or 39.06 kHz), so that an audio sound wave around 2 kHz (or 1 kHz) is generated. The FPGA has a clock rate of 50 MHz, which means that the phase difference between channels can be realized by the time shifting of signals with a high resolution of only 0.02 μs. The weight coefficients of each channel can be controlled by the input voltage for MOSFET drivers.

The experiments were conducted in a full anechoic room at Nanjing University with dimensions of 11.4 m × 7.8 m × 6.7 m (height). The relative humidity and temperature were 52% and 26 °C, respectively. A photo of the experiment setup is presented in Fig. 13(c). The parametric source was mounted on a turntable system (Brüel & Kjær Type 9640). The audio sound directivity for a parametric source is defined in its inverse-law far field, typically situated more than 10 m away from the source [8]. However, conducting measurements at such a large distance is challenging in experiments due to the alignment error and the limited size of the anechoic room. As a trade-off, a condenser microphone (Brüel & Kjær Type 4135) was used to measure the sound pressure at 3 m away from the parametric source. The signal is conditioned (Brüel & Kjær Type 2690) and analyzed by a PULSE analyzer (Brüel & Kjær Type 3160). To avoid spurious sound induced by the intensive ultrasounds [38], the microphone was covered by a piece of small and thin plastic film. The preliminary experiment results show that the insertion loss of this plastic film is more than 20 dB at 40 kHz, which effectively blocks the ultrasound, and less than 1.5 dB at 1 kHz and 2 kHz, causing a little impact on the audio sound.

Fig. 14 shows the directivity patterns generated by both uniform and optimal array configurations with 8 channels, measured between 0° and 180° with a resolution of 1°. Fig. 15 presents the results generated by the 16-channel parametric sources. For better comparison, the measured results are normalized to the SPL at the main lobe. For a uniform 8-channel array generating
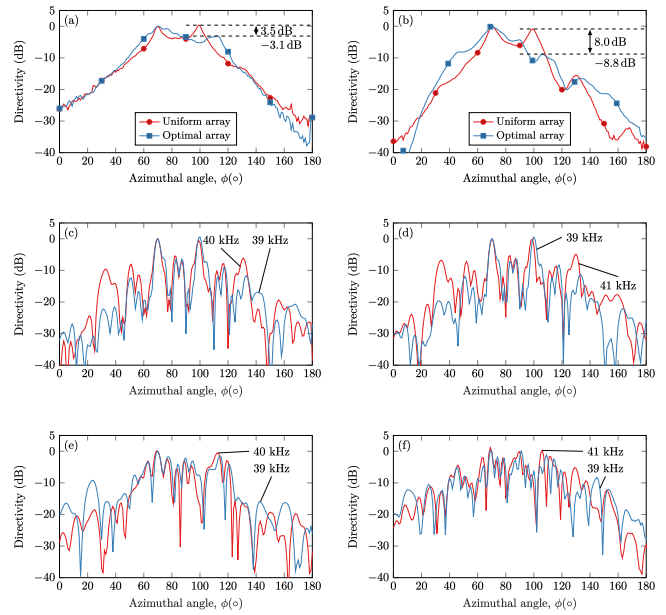

Fig. 14. Directivities measured at 3 m generated by 8-channel steerable parametric sources. The ultrasound directivities generated by the (c) uniform and (e) optimal array for the audio sound directivity shown in (a) at 1 kHz. The ultrasound directivities generated by the (d) uniform and (f) optimal array for the audio sound directivity shown in (b) at 2 kHz.
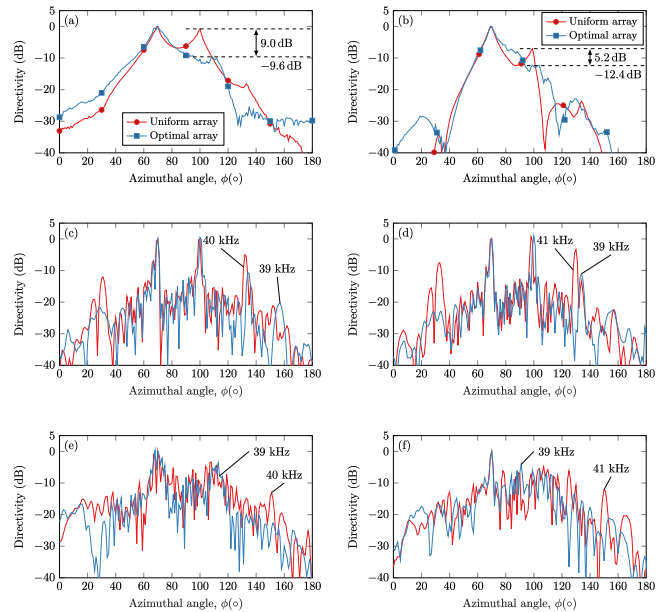

Fig. 15. Directivities measured at 3 m generated by 16-channel steerable parametric sources. The ultrasound directivities generated by the (c) uniform and (e) optimal array for the audio sound directivity shown in (a) at 1 kHz. The ultrasound directivities generated by the (d) uniform and (f) optimal array for the audio sound directivity shown in (b) at 2 kHz.

audio sound at 2 kHz as shown in Fig. 14(b), it is observed that the directivity achieves three local peaks of 0 dB, −0.9 dB, and −15.6 dB at 70°, 99°, and 130°, respectively. In the simulation shown in Fig. 3(d), three local peaks of 0 dB, 1.3 dB, and −20.8 dB, are achieved at 70°, 99.1°, and 135.7°, respectively. Although the magnitude of the two grating lobes do not match

the simulation results, the location of these three local peaks is well predicted. The measured directivity generated by the optimal 8-channel array configuration in Figs. 14(b) shows that the grating lobe at $99°$ decreases by 8 dB. This improvement can be explained by observing the measured ultrasound directivities for the uniform and optimal array configurations in Figs. 14(d) and (f), respectively. For the uniform array, the peaks around $99°$ in two ultrasound directivities are seen to approximately coincide with each other so their product is significant causing a grating lobe at this direction. For the optimal array, Fig. 14(f) shows that the sparse array results in a null of one ultrasound directivity around $99°$ where the grating lobe of the other ultrasound directivity appears. This is in accordance with the simulation results presented in Figs. 3(b) and 4(b).

At a lower audio frequency at 1 kHz, the performance of the sidelobe reduction deteriorates as shown in Fig. 14(a). Compared to the case at 2 kHz, the PSL increases from -8.8 dB to -3.1 dB. This is in accordance with the simulations presented in Figs. 6 and 7. This deterioration in performance is also observed for the 16-channel array by comparing Figs. 15(a) and (b), where the PSL of the audio directivity increases from -12.4 dB to -9.6 dB as the audio frequency decreases from 2 kHz to 1 kHz. The reason behind this is that the Westervelt directivity becomes broader at lower audio frequencies. Fortunately, this deterioration can be addressed to some extent by increasing the number of array elements. By comparing Figs. 14(a) and 15(a), the PSL decreases from -3.1 dB to -9.6 dB at 1 kHz by doubling the number of elements.

The aforementioned experimental results illustrate the successful suppression of the sidelobe as well as the grating lobe in the audio sound directivity generated by a parametric source through the utilization of a sparse random array. However, the achieved performance falls short of the predicted results. For instance, the measured PSL of the optimal 8-channel array at 2 kHz is -8.8 dB, as shown in Fig. 14(b), while the prediction in Fig. 4(d) suggests a value of -15.5 dB. Several factors could contribute to this disparity. Firstly, the convolution model (2) employed in this work for calculating the far field directivity is inaccurate at large aperture sizes and audio frequencies due to the omission of the aperture effect of audio sound [39]. Secondly, the validity of the convolution model is restricted to 2D physical models requiring that the dimension of the array without the phase modulation is much larger than both the ultrasound and audio sound wavelengths [39], but the dimension of the experimental prototypes (8 cm) is smaller than the latter (e.g., 34.3 cm at 1 kHz). Moreover, the audio sound directivity generated by a parametric source is defined in the inverse-law far field, which is typically more than 10 m away from the source [8]. Due to alignment errors and the limited space of the anechoic room, measuring the directivity at such distances is challenging. Consequently, the directivity was measured at a distance of only 3 m during the experiments. It is worth noting that the audio sound can exhibit a broader directivity in the near field, as demonstrated in [14]. A promising solution might be optimizing the directivity in the near field, but the computational cost is quite heavy at present. Lastly, discrepancies in the amplitude and phase response among ultrasonic emitters in each channel can also contribute to errors. Although these issues necessitate substantial further research, the measured results presented in this study effectively show the efficacy of the sparse array technique in suppressing the sidelobe and the grating lobe in the audio sound directivity generated by a parametric source.

V. CONCLUSION

This article proposes optimal designs for suppressing sidelobes generated by a steerable parametric source using a sparse random array technique similar to that previously applied to antenna and medical ultrasound arrays. The position and weight coefficients of the array elements are optimized using the SA algorithm, where the objective is to minimize the peak sidelobe level of the directivity pattern. It is shown that the sidelobe including grating lobes generated by a steerable parametric source can be suppressed even if the interelement separation fails to satisfy the Nyquist criterion. However, suppression performance is seen to deteriorate at low audio and high ultrasound frequencies due to the effects of Westervelt directivity, although this performance can be improved by increasing the element number. The sidelobe suppression is achieved when the array elements are optimally spaced and the wave amplitudes are optimally weighted, so that the emitted sound waves arrive randomly at the grating lobe while they still arrive in-phase at the main lobe. This work certainly open new perspectives for the optimal design of a steerable parametric source. It provides a practical and efficient way to minimize the sidelobes generated by a sparse parametric source array. While the effects of the ultrasound frequency have been investigated through simulations, as depicted in Fig. 8, they have not been verified through measurements due to the limited response of the ultrasonic emitters employed in this study. In light of this, it is crucial to explore this aspect in future research, as other ultrasonic frequencies are also utilized in applications, such as 60 kHz and 80 kHz. It is also worth mentioning that the positions and weight coefficients of array elements are optimized specifically for a particular audio frequency in this work. To reduce the sidelobe level for a wideband audio signal, the wideband directivity can be used as the objective function in (11). The sparse random array technique would still work for the wideband signal, but the performance of the reduction might deteriorate due to additional constraints in the optimization.

REFERENCES

[1] W.-S. Gan, J. Yang, and T. Kamakura, "A review of parametric acoustic array in air," *Appl. Acoust.*, vol. 73, no. 12, pp. 1211–1219, 2012.

[2] N. Tanaka and M. Tanaka, "Active noise control using a steerable parametric array loudspeaker," *J. Acoust. Soc. Amer.*, vol. 127, no. 6, pp. 3526–3537, 2010.

[3] C. Shi, Y. Kajikawa, and W.-S. Gan, "An overview of directivity control methods of the parametric array loudspeaker," *APSIPA Trans. Signal Inf. Process.*, vol. 3, pp. 1–12, 2014.

[4] K. C.-M. Lee and W.-S. Gan, "Bandwidth-efficient recursive pth-order equalization for correcting baseband distortion in parametric loudspeakers," *IEEE/ACM Trans. Audio, Speech, Lang. Process.*, vol. 14, no. 2, pp. 706–710, Mar. 2006.

[5] Y. Mu, P. Ji, W. Ji, M. Wu, and J. Yang, "Modeling and compensation for the distortion of parametric loudspeakers using a one-dimension volterra filter," *IEEE/ACM Trans. Audio, Speech, Lang. Process.*, vol. 22, no. 12, pp. 2169–2181, Dec. 2014.

[6] Y. Hatano, C. Shi, and Y. Kajikawa, "Compensation for nonlinear distortion of the frequency modulation-based parametric array loudspeaker," *IEEE/ACM Trans. Audio, Speech, Lang. Process.*, vol. 25, no. 8, pp. 1709–1717, Aug. 2017.

[7] P. Ji, E.-L. Tan, W.-S. Gan, and J. Yang, "A comparative analysis of pre-processing methods for the parametric loudspeaker based on the khokhlov equation for speech reproduction," *IEEE/ACM Trans. Audio, Speech, Lang. Process.*, vol. 19, no. 4, pp. 937–946, May 2011.

[8] J. Zhong, R. Kirby, and X. Qiu, "The near field, westervelt far field, and inverse-law far field of the audio sound generated by parametric array loudspeakers," *J. Acoust. Soc. Amer.*, vol. 149, no. 3, pp. 1524–1535, 2021.

[9] Y. Kagawa, T. Tsuchiya, T. Yamabuchi, H. Kawabe, and T. Fujii, "Finite element simulation of non-linear sound wave propagation," *J. Sound Vib.*, vol. 154, no. 1, pp. 125–145, Apr. 1992.

[10] M. Červenka and M. Bednařík, "A versatile computational approach for the numerical modelling of parametric acoustic array," *J. Acoust. Soc. Amer.*, vol. 146, no. 4, pp. 2163–2169, 2019.

[11] J. Yang, K. Sha, W.-S. Gan, and J. Tian, "Modeling of finite-amplitude sound beams: Second order fields generated by a parametric loudspeaker," *IEEE Trans. Ultrason., Ferroelect., Freq. Control*, vol. 52, no. 4, pp. 610–618, Apr. 2005.

[12] M. Červenka and M. Bednařík, "Non-paraxial model for a parametric acoustic array," *J. Acoust. Soc. Amer.*, vol. 134, no. 2, pp. 933–938, 2013.

[13] J. Zhong, R. Kirby, and X. Qiu, "A spherical expansion for audio sounds generated by a circular parametric array loudspeaker," *J. Acoust. Soc. Amer.*, vol. 147, no. 5, pp. 3502–3510, 2020.

[14] J. Zhong, R. Kirby, M. Karimi, and H. Zou, "A cylindrical expansion of the audio sound for a steerable parametric array loudspeaker," *J. Acoust. Soc. Amer.*, vol. 150, no. 5, pp. 3797–3806, 2021.

[15] P. J. Westervelt, "Parametric acoustic array," *J. Acoust. Soc. Amer.*, vol. 35, no. 4, pp. 535–537, 1963.

[16] H. O. Berktay, "Possible exploitation of non-linear acoustics in underwater transmitting applications," *J. Sound Vib.*, vol. 2, no. 4, pp. 435–461, 1965.

[17] H. O. Berktay and D. J. Leahy, "Farfield performance of parametric transmitters," *J. Acoust. Soc. Amer.*, vol. 55, no. 3, pp. 539–546, 1974.

[18] W.-S. Gan, J. Yang, K.-S. Tan, and M.-H. Er, "A digital beamsteerer for difference frequency in a parametric array," *IEEE/ACM Trans. Audio, Speech, Lang. Process.*, vol. 14, no. 3, pp. 1018–1025, May 2006.

[19] C. Shi and W.-S. Gan, "Product directivity models for parametric loudspeakers," *J. Acoust. Soc. Amer.*, vol. 131, no. 3, pp. 1938–1945, 2012.

[20] O. Guasch and P. Sánchez-Martín, "Far-field directivity of parametric loudspeaker arrays set on curved surfaces," *Appl. Math. Model.*, vol. 60, pp. 721–738, 2018.

[21] C. Shi and Y. Kajikawa, "A convolution model for computing the far-field directivity of a parametric loudspeaker array," *J. Acoust. Soc. Amer.*, vol. 137, no. 2, pp. 777–784, 2015.

[22] C. Shi, Y. Wang, H. Xiao, and H. Li, "Extended convolution model for computing the far-field directivity of an amplitude-modulated parametric loudspeaker," *J. Phys. D. Appl. Phys.*, vol. 55, no. 24, 2022, Art. no. 244002.

[23] C. Shi and W.-S. Gan, "Grating lobe elimination in steerable parametric loudspeaker," *IEEE Trans. Ultrason., Ferroelect., Freq. Control*, vol. 58, no. 2, pp. 437–450, Feb. 2011.

[24] C. Shi, Y. Kajikawa, and W.-S. Gan, "Generating dual beams from a single steerable parametric loudspeaker," *J. Acoust. Soc. Amer.*, vol. 99, pp. 43–50, 2015.

[25] S. A. Goss, L. A. Frizzell, J. T. Kouzmanoff, J. M. Barich, and J. M. Yang, "Sparse random ultrasound phased array for focal surgery," *IEEE Trans. Ultrason., Ferroelect., Freq. Control*, vol. 43, no. 6, pp. 1111–1121, Nov. 1996.

[26] D. G. Kurup, M. Himdi, and A. Rydberg, "Synthesis of uniform amplitude unequally spaced antenna arrays using the differential evolution algorithm," *IEEE Trans. Antennas Propag.*, vol. 51, no. 9, pp. 2210–2217, Sep. 2003.

[27] V. Murino, A. Trucco, and C. Regazzoni, "Synthesis of unequally spaced arrays by simulated annealing," *IEEE Trans. Signal Process.*, vol. 44, no. 1, pp. 119–122, Jan. 1996.

[28] H. Xue, X. Zhang, X. Guo, J. Tu, and D. Zhang, "Optimization of a random linear ultrasonic therapeutic array based on a genetic algorithm," *Ultrasonics*, vol. 124, Apr. 2022, Art. no. 106751.

[29] M. M. Khodier and C. G. Christodoulou, "Linear array geometry synthesis with minimum sidelobe level and null control using particle swarm optimization," *IEEE Trans. Antennas Propag.*, vol. 53, no. 8, pp. 2674–2679, Aug. 2005.

[30] S. Kirkpatrick, C. D. Gelatt, and M. P. Vecchi, "Optimization by simulated annealing," *Science*, vol. 220, no. 4598, pp. 671–680, May 1983.

[31] M. R. Bai, P.-J. Hsieh, and K.-N. Hur, "Optimal design of minimum mean-square error noise reduction algorithms using the simulated annealing technique," *J. Acoust. Soc. Amer.*, vol. 125, no. 2, pp. 934–943, Feb. 2009.

[32] S.-C. Wooh and Y. Shi, "Three-dimensional beam directivity of phase-steered ultrasound," *J. Acoust. Soc. Amer.*, vol. 105, no. 6, pp. 3275–3282, Jun. 1999.

[33] L. W. Schmerr Jr., *Fundamentals of Ultrasonic Phased Arrays*. Berlin, Germany: Springer, 2014.

[34] *Acoustics Attenuation of sound During Propagation Outdoors Part 1: Calculation of the Absorption of Sound by the Atmosphere*, ISO Standard 9613-1:1993, International Organization for Standardization, Geneva, Switzerland, 1993.

[35] P. J. Bevelacqua and C. A. Balanis, "Minimum sidelobe levels for linear arrays," *IEEE Trans. Antennas Propag.*, vol. 55, no. 12, pp. 3442–3449, Dec. 2007.

[36] A. Marzo, T. Corkett, and B. W. Drinkwater, "Ultraino: An open phased-array system for narrowband airborne ultrasound transmission," *IEEE Trans. Ultrason., Ferroelectr. Freq. Control*, vol. 65, no. 1, pp. 102–111, Jan. 2018.

[37] J. Zhong et al., "Low frequency audio sound field generated by a focusing parametric array loudspeaker," *IEEE Trans. Audio Speech Lang. Process.*, vol. 30, pp. 3098–3109, 2022.

[38] P. Ji and J. Yang, "An experimental investigation about parameters' effects on spurious sound in parametric loudspeaker," *Appl. Acoust.*, vol. 148, pp. 67–74, 2019.

[39] J. Zhong, H. Zou, J. Lu, and D. Zhang, "A modified convolution model for calculating the far field directivity of a parametric array loudspeaker," *J. Acoust. Soc. Amer.*, vol. 153, no. 3, pp. 1439–1451, 2023.